Published in final edited form as:
*IEEE Trans Med Imaging*. 2015 February ; 34(2): 678–689. doi:10.1109/TMI.2014.2365179.

# Regularization Designs for Uniform Spatial Resolution and Noise Properties in Statistical Image Reconstruction for 3D X-ray CT

**Jang Hwan Cho [Member, IEEE]** and **Jeffrey A. Fessler [Fellow, IEEE]**
the Department of Electrical Engineering and Computer Science, University of Michigan, Ann Arbor, MI 48105 USA

Jang Hwan Cho: janghcho@umich.edu; Jeffrey A. Fessler: fessler@umich.edu

## Abstract

Statistical image reconstruction methods for X-ray computed tomography (CT) provide improved spatial resolution and noise properties over conventional filtered back-projection (FBP) reconstruction, along with other potential advantages such as reduced patient dose and artifacts. Conventional regularized image reconstruction leads to spatially variant spatial resolution and noise characteristics because of interactions between the system models and the regularization. Previous regularization design methods aiming to solve such issues mostly rely on circulant approximations of the Fisher information matrix that are very inaccurate for undersampled geometries like short-scan cone-beam CT. This paper extends the regularization method proposed in [1] to 3D cone-beam CT by introducing a hypothetical scanning geometry that helps address the sampling properties. The proposed regularization designs were compared with the original method in [1] with both phantom simulation and clinical reconstruction in 3D axial X-ray CT. The proposed regularization methods yield improved spatial resolution or noise uniformity in statistical image reconstruction for short-scan axial cone-beam CT.

### Index Terms

regularization; model-based image reconstruction; cone-beam tomography; iterative reconstruction

## I. Introduction

Statistical image reconstruction methods for X-ray computed tomography (CT) use realistic models that incorporate the statistical properties of the noise and the physics of the data acquisition system [2]. Compared to conventional filtered back-projection (FBP) reconstruction, statistical methods are more accurate and are more flexible for modeling different kinds of physical constraints. Potential advantages of statistical image reconstruction methods over FBP reconstruction have been demonstrated in terms of noise, resolution, and artifacts [3]–[5]. Such improvements in image quality become more apparent in low-dose scans where FBP reconstruction suffers from increased streak artifacts [6]. However, many factors need to be addressed to ensure the success of statistical methods in

clinical applications. Diagnostic readability of the reconstructed images depends on various characteristics such as texture, resolution, noise, and artifacts. In particular, uniformity of the resolution or noise characteristics throughout the reconstructed image is desirable. This paper proposes new space-variant regularization designs that yield reconstructed images with improved uniformity of resolution or noise.

Regularization is necessary to control noise since unregularized image reconstruction leads to excessively noisy images. By integrating a penalty term into the objective function, regularized image reconstruction methods, such as penalized-likelihood (PL) methods or penalized weighted least squares (PWLS) methods, provide controlled noise and resolution properties in the reconstructed image. However, interactions between the regularization, system models, and statistical weighting cause the reconstructed images to have object-dependent nonuniform and anisotropic spatial resolution and noise properties, even for idealized shift-invariant imaging systems [1]. Nonuniformity becomes severe for short-scans in cone-beam CT (CBCT), having angular spans of $\pi + 2\gamma$ where $\gamma$ is the fan angle of the detector, compared to full scans, and also for undersampled voxels[1] in 3D axial or helical scanning geometries. In [1], a regularizer based on the aggregated certainty was developed for 2D PET to yield images with approximately uniform spatial resolution, and that regularizer has been used for other geometries and modalities [9]–[13]. However, the aggregated certainty regularizer does not provide uniform resolution when applied to modalities such as 2D short-scan fan-beam CT or 3D cone beam CT because of asymmetric scan geometries caused by short-scan orbits or cone-angle effects or both. In [10] and [12], the original aggregated certainty regularizer was modified with a diagonal scaling factor for 3D PET. Recently, it was also extended to both static and multi-frame reconstruction in 3D PET by considering spatially variant and frame-dependent sensitivity [14]. Since the term “aggregated certainty” is less apt for some imaging modalities such as CT, instead, we use the more general term “pre-tuned spatial strength”, which represents that the purpose of the function is to control the regularization strength at each voxel, before the reconstruction process, so that the reconstructed image is guided to have desired characteristics, *i.e.*, uniform resolution.

Many previous regularization design methods focussed on choosing directional coefficients in the regularizer by matching local characteristics, such as impulse response or correlation function, of the estimator to target characteristics to achieve uniform and isotropic resolution [15]–[17] or noise characteristics [18], [19]. Since both the global regulation parameters) and the pre-tuned spatial strengths can be incorporated into directional regularizer coefficients, those regulation design methods are more general and flexible than simply adjusting the regulation strength at each voxel. However, such design methods require additional computations to design the coefficients for every voxel, and it is challenging to obtain both uniformity and isotropy at the same time for either spatial resolution or noise characteristics. Especially for the undersampled voxels in cone-beam CT, locally circulant approximations of the Fisher information matrix are very inaccurate, leading to imperfect

[1]In this study, “full” sampling does not refer to the complete sampling conditions derived in [7], [8], but rather that the voxel is seen in every projection view. Thus, “undersampling” indicates the voxel is seen in only some of the projection views.

coefficient designs at such locations. Furthermore, the memory requirement to store all directional coefficients for every voxel can be burdensome.

This paper extends [1] by proposing a modified pre-tuned spatial strength function for 3D CT that yields improved resolution uniformity throughout the reconstructed image including undersampled voxel locations. We also propose a shift-variant regularizer that provides approximately uniform noise characteristics in the reconstructed image. Section II reviews the system models for statistical image reconstruction and some fundamental concepts such as estimator local impulse response (LIR) and covariance. Section III proposes new regularizes by generalizing the system matrix using a hypothetical geometry concept. Two different regularizers are presented that yield improved uniform resolution or noise characteristics in the reconstructed image, respectively. Section IV presents results using both simulated and real clinical X-ray CT data. Section V concludes by summarizing the contributions of this study and suggesting potential future work.

## II. Spatial Resolution and Noise Properties of Statistical Image Reconstruction

This section first reviews statistical image reconstruction in terms of the system models for a penalized weighted least squares (PWLS) formulation. The concept of local impulse response and estimator covariance is also reviewed, and metrics for analyzing spatial resolution and noise properties in the reconstructed image are discussed.

### A. Statistical Image Reconstruction

Noisy CT sinogram measurements can be expressed as a discrete vector, $\boldsymbol{y} = (y_1 \ldots, y_{n_\mathrm{d}})$, where $y_i$ represents the $i$th line integral through the object for a given scanning geometry. These sinogram measurements are related to recorded detector measurements, $\boldsymbol{I} = (I_1, \ldots, I_{n_\mathrm{d}})$, by the Beer-Lambert law [20]. For simplicity, we use the following statistical model for the detector measurements under the mono-energetic assumption

$$E[I_i] = \bar{I}_i = b_i \exp(-[\boldsymbol{A}\boldsymbol{x}]_i) + r_i,$$

where $\boldsymbol{A}$ is the system matrix, $\boldsymbol{x} = (x_1, \ldots, x_{n_\mathrm{p}})$ is the discrete vector of the imaged object, $[\boldsymbol{A}\boldsymbol{x}]_i = \sum_{j=1}^{n_\mathrm{p}} a_{ij} x_j$, $b_i$ is the X-ray source intensity for $i$th ray, and $r_i$ denotes the background contributions from factors such as scatter and crosstalk.

The measurement noise statistics can be modeled using a probability density function by relating the measurements $y_i$ to their mean values $E[y_i]$, and are mainly affected by physical processes in the data acquisition system. For integrating detectors, the statistics of X-ray measurements is a complicated mixture of compound Poisson photon distribution and Gaussian electronic noise [21], [22]. In practice, the following simple models have been used successfully. A Poisson model for pre-log data $I_i$ can be written as [23]

$$I_i \sim \text{Poisson}\left\{b_i \exp(-[\boldsymbol{A}\boldsymbol{x}]_i) + r_i\right\}. \quad (1)$$

A quadratic approximation of the negative log-likelihood of (1) implies that the post-log data $y_i$ is a approximately Gaussian random variable [24], [25]

$$y_i \sim N\left([\boldsymbol{A}\boldsymbol{x}]_i, \frac{\bar{I}_i}{\left(\bar{I}_i - r_i\right)^2}\right). \quad (2)$$

CT image reconstruction often is formulated as a minimization problem with a PWLS cost function of the form

$$\Psi(\boldsymbol{x}) = \mathrm{L}(\boldsymbol{x}) + \mathrm{R}(\boldsymbol{x}),\ \mathrm{L}(\boldsymbol{x}) = \frac{1}{2}\|\boldsymbol{y} - \boldsymbol{A}\boldsymbol{x}\|_{\boldsymbol{W}}^2 \quad (3)$$

$$\hat{\boldsymbol{x}} = \arg\min_{\boldsymbol{x}} \Psi(\boldsymbol{x}), \quad (4)$$

where $\mathrm{R}(\boldsymbol{x})$ is a regularizer that controls the spatial resolution and noise characteristics in the reconstructed image typically by penalizing local differences between voxels, and $\boldsymbol{W} = \boldsymbol{D}[w_i] \triangleq \mathrm{diag}\{w_i\}$ is a statistical weighting matrix. (We assume the measurements are independent so the data covariance is diagonal.) The coefficients $\{w_i\}$ of the statistical weighting matrix should be the reciprocal of the variances of the measurements by the Gauss-Markov theorem [26]:

$$w_i \triangleq \frac{1}{\sigma^2(E[y_i])} = \frac{(\bar{I}_i - r_i)^2}{\bar{I}_i}.$$

In practice, the means of the measurements are unknown so typically the weights are estimated by a plug-in approach, *i.e.*, $w_i \approx 1/\sigma^2(y_i)$ for transmission tomography. The ideas in this paper generalize readily to other penalized-likelihood formulations [27].

We consider regularizers having the following form:

$$\mathrm{R}(\boldsymbol{x}) = \sum_{j=1}^{n_\mathrm{p}} \kappa_j \sum_{l=1}^{N_1} \kappa_{j-j_l} \beta_l \psi_l((c_l * * * x)[n, m, z]), \quad (5)$$

where $N_1$, is the size of the neighborhood, $j_l$ denotes the offset of the $l$th neighbor in lexicographical order, $\beta_l$ is a regulation parameter that balances between the data-fitting term and the regularizer [28], $\kappa_j$ is a user-defined value that controls local spatial resolution and noise in the reconstructed image [1, eqn. (35)], $\psi_l$ is a potential function, * * * denotes 3-D convolution. We define a first-order differencing function that penalizes $l$th neighbor as

$$c_l[n,m,z]=\frac{\delta[n,m,z]-\delta[n-n_l,m-m_l,z-z_l]}{\sqrt{n_l^2+m_l^2+z_l^2}},$$

where $\delta[n, m, z]$ is the Kronecker impulse at location [0, 0, 0], and $n_l$, $m_l$, $z_l$ denote the offset of the $l$th neighbor. The regulation parameter $\beta_l$ is usually determined based on data-independent factors like voxel sizes, and a typical choice is $\beta_l = 1, \forall l$. The parameter also can be selected more systematically as in [28].

The goal of this paper is to refine the regularizer R($\boldsymbol{x}$) by designing $\{\kappa_j\}$ so that the reconstructed image has more uniform resolution or noise properties. We want to improve upon the design proposed in [1] which was

$$\kappa_j=\sqrt{\frac{\sum_{i=1}^{n_\mathrm{d}}a_{ij}^2 w_i}{\sum_{i=1}^{n_\mathrm{d}}a_{ij}^2}}. \quad (6)$$

### B. CRC and Ensemble Variance

The local impulse response describes the local spatial resolution properties. We used the following definition of local impulse response at the $j$th voxel [16]:

$$l_j \triangleq \lim_{\varepsilon\to 0}\frac{\hat{\boldsymbol{x}}\left(\overline{\boldsymbol{y}}\left(\boldsymbol{x}^{\mathrm{true}}+\varepsilon\boldsymbol{\delta}_j\right)\right)-\hat{\boldsymbol{x}}\left(\overline{\boldsymbol{y}}\left(\boldsymbol{x}^{\mathrm{true}}\right)\right)}{\varepsilon} \quad (7)$$

$$=\nabla_{\boldsymbol{y}}\hat{\boldsymbol{x}}(\boldsymbol{y})|_{\boldsymbol{y}=\overline{\boldsymbol{y}}(\boldsymbol{x}^{\mathrm{true}})}\nabla_{\boldsymbol{x}}\overline{\boldsymbol{y}}(\boldsymbol{x})|_{\boldsymbol{x}=\boldsymbol{x}^{\mathrm{true}}}\boldsymbol{\delta}_j, \quad (8)$$

where $\boldsymbol{\delta}_j$ is a Kronecker impulse at the $j$th voxel, and the gradient operations are matrices with the following elements:

$$[\nabla_{\boldsymbol{y}}\hat{\boldsymbol{x}}(\boldsymbol{y})]_{ji}=\frac{\partial}{\partial y_i}\hat{x}_j(\boldsymbol{y}), [\nabla_{\boldsymbol{x}}\overline{\boldsymbol{y}}(\boldsymbol{x})]_{ij}=\frac{\partial}{\partial x_j}\overline{y}_i(\boldsymbol{x}).$$

For simplicity we focus on quadratic regularization, for which, from (8), the local impulse response of the PWLS estimator (4) is expressed as

$$\boldsymbol{l}_j=\left[\boldsymbol{A}'\boldsymbol{W}\boldsymbol{A}+\boldsymbol{R}\right]^{-1}\boldsymbol{A}'\boldsymbol{W}\boldsymbol{A}\boldsymbol{\delta}_j, \quad (9)$$

where $\boldsymbol{R}$ is the Hessian of the regularizer R($\boldsymbol{x}$) [1].

One common metric for measuring the local resolution is the width of the local impulse response at the $j$th voxel, such as the full width half maximum (FWHM) [1]. Alternatively,

the peak amplitude of the local impulse response, called the contrast recovery coefficient (CRC) [9], can be used to quantify resolution

$$\mathrm{CRC}(\boldsymbol{l}_j) \triangleq \boldsymbol{\delta}_j^T \boldsymbol{l}_j = \boldsymbol{\delta}_j^T [\boldsymbol{A}' \boldsymbol{W} \mathbf{A} + \boldsymbol{R}]^{-1} \boldsymbol{A}' \boldsymbol{W} \boldsymbol{A} \boldsymbol{\delta}_j. \quad (10)$$

To measure isotropy of an impulse response, the width measure is more effective. On the other hand, uniformity of the impulse responses is easier to assess with the CRC. In this paper, we use the CRC of the local impulse response to quantify spatial resolution.

With a quadratic regularizer, the closed-form solution of (4) is given by

$$\hat{\boldsymbol{x}} = (\boldsymbol{A}' \boldsymbol{W} \boldsymbol{A} + \boldsymbol{R})^{-1} \boldsymbol{A}' \boldsymbol{W} \boldsymbol{y}. \quad (11)$$

The covariance of the reconstructed image $\hat{\boldsymbol{x}}$ [26] is

$$\mathrm{cov}(\hat{\boldsymbol{x}}) = (\boldsymbol{A}' \boldsymbol{W} \boldsymbol{A} + \boldsymbol{R})^{-1} \boldsymbol{A}' \boldsymbol{W} \mathrm{cov}(\boldsymbol{y}) \boldsymbol{W} \boldsymbol{A} (\boldsymbol{A}' \boldsymbol{W} \boldsymbol{A} + \boldsymbol{R})^{-1}. \quad (12)$$

If the weighting is chosen such that $\mathrm{cov}(\boldsymbol{y}) = \boldsymbol{W}^{-1}$, then the reconstructed image covariance simplifies to

$$\mathrm{cov}(\hat{\boldsymbol{x}}) = (\boldsymbol{A}' \boldsymbol{W} \boldsymbol{A} + \boldsymbol{R})^{-1} \boldsymbol{A}' \boldsymbol{W} \boldsymbol{A} (\boldsymbol{A}' \boldsymbol{W} \boldsymbol{A} + \boldsymbol{R})^{-1}. \quad (13)$$

However, in some cases, additional factors are applied to $\boldsymbol{W}$. For instance, Parker weighting [29] is applied to sinogram measurements for short-scan FBP reconstruction. It may also be used in iterative reconstructions so that the temporal resolution of such reconstructions matches that of FBP reconstruction. Such modifications change the statistical characteristics of $\boldsymbol{W}$ and it no longer satisfies $\mathrm{cov}(\boldsymbol{y}) = \boldsymbol{W}^{-1}$ We can express the statistical weighting more generally as

$$\boldsymbol{W} = \hat{\boldsymbol{W}} \boldsymbol{V} = \boldsymbol{D}[\hat{W}_i v_i], \quad (14)$$

where the weighting $\hat{\boldsymbol{W}}$ is the conventional choice that satisfies $\hat{w}_i = 1/\mathrm{Var}\{y_i\}$, and $\{v_i\}$ denotes additional weighting elements. The reconstructed image covariance (12) with such statistical weighting can be expressed as follows

$$\mathrm{cov}(\hat{\boldsymbol{x}}) = (\boldsymbol{A}' \boldsymbol{W} \boldsymbol{A} + \boldsymbol{R})^{-1} \boldsymbol{A}' \breve{\boldsymbol{W}} \boldsymbol{A} (\boldsymbol{A}' \boldsymbol{W} \boldsymbol{A} + \boldsymbol{R})^{-1}, \quad (15)$$

where $\breve{\boldsymbol{W}} = \boldsymbol{V} \hat{\boldsymbol{W}} \boldsymbol{V} = \boldsymbol{D}[\hat{W}_i v_i^2]$.

The noise property of the estimator can be quantified with the ensemble variance at each voxel:

$$\mathrm{var}(\hat{\boldsymbol{x}}_j) = \boldsymbol{\delta}_j^T (\boldsymbol{A}' \boldsymbol{W} \boldsymbol{A} + \boldsymbol{R})^{-1} \boldsymbol{A}' \breve{\boldsymbol{W}} \boldsymbol{A}' (\boldsymbol{A}' \boldsymbol{W} \boldsymbol{A} + \boldsymbol{R})^{-1} \boldsymbol{\delta}_j. \quad (16)$$

The entire *j*th column of the covariance matrix (15) represents the noise correlation of the *j*th voxel in the reconstructed image with all other voxels

$$\mathrm{corr}(\hat{\boldsymbol{x}}_j) \triangleq (\boldsymbol{A}' \boldsymbol{W} \boldsymbol{A} + \boldsymbol{R})^{-1} \boldsymbol{A}' \breve{\boldsymbol{W}} \boldsymbol{A} (\boldsymbol{A}' \boldsymbol{W} \boldsymbol{A} + \boldsymbol{R})^{-1} \boldsymbol{\delta}_j. \quad (17)$$

Our goal is to design regularizes for which $\boldsymbol{l}_j$ or corr($\boldsymbol{x}_j$)^ are approximately uniform over the 3D object.

## III. New Regularization Designs

This section reviews the aggregated certainty regularizer developed in [1], and then develops new regularization designs that provide approximately uniform resolution or noise properties by using an "ideal" system matrix factorization.

### A. System matrix augmentation using a hypothetical geometry

The aggregated certainty regularizer in [1] was developed for shift-invariant systems like 2D PET. For shift-variant systems like CBCT, the formulation in [1] must be modified.

The Fisher information matrix $\boldsymbol{A}'\boldsymbol{W}\boldsymbol{A}$ is shift-variant for both emission and transmission tomography, causing nonuniform properties of the reconstructed image. Statistical weighting is only partially responsible for the nonuniformity; even in the unweighted case, the Fisher information matrix $\boldsymbol{A}'\boldsymbol{A}$ is also shift-variant for 3D PET and CT. In [1], the system matrix $\boldsymbol{A}$ was factored into three elements as follows

$$a_{ij} = c_i g_{ij} s_j, \quad (18)$$

where $\{c_i\}$ denote ray-dependent factors, $\{s_j\}$ denote voxel-dependent factors, and $\boldsymbol{G} = [g_{ij}]$ represents the object-independent geometric portion of the tomographic system response. Ideally we would like to choose $\{c_i\}$ and $\{s_j\}$ and $\boldsymbol{G}$ such that $\boldsymbol{G}'\boldsymbol{G}$ is shift-invariant. So it can be accurately approximated with a circulant matrix (implemented via a fast Fourier transform (FFT)), leading to improved regularizer designs. The matrix representation of (18) is

$$\boldsymbol{A} = \boldsymbol{D}[c_i] \boldsymbol{G} \boldsymbol{D}[s_j]. \quad (19)$$

Since this representation is not unique, we can try to design each of the factors to make $\boldsymbol{G}'\boldsymbol{G}$ "very shift-invariant". The original design presented in [1] for PET assumed uniform voxel-dependent factors, *i.e.*, $s_j = 1, \forall j$, and the ray-dependent part included only non-geometric aspects such as detector efficiency and dead time. In 2D PET, this leads to geometric factors $\{g_{ij}\}$ for which $\boldsymbol{G}'\boldsymbol{G}$ is nearly shift-invariant. However, this conventional choice of $\boldsymbol{G}$ leads to $\boldsymbol{G}'\boldsymbol{G}$ that is highly shift-variant for 3D cone beam CT and even for 2D fan-beam CT for short-scan geometries.

Here, we present a new generalization of (18) that works in various geometries including 3D cone beam CT. First, we consider the geometric sampling properties of $\boldsymbol{A}$ and consider what rays are "missing" that cause $\boldsymbol{A}'\boldsymbol{A}$ to be shift-variant. For example, in a short-scan fan-beam geometry we are missing some of the views that would have been acquired with a full 360° scan. As another example, for a CBCT axial scan, we are missing the data that would have been acquired with a "step and shoot" set of axial scans. For axial CBCT with a full 360° scan, $\boldsymbol{A}'\boldsymbol{A}$ is approximately shift-invariant over the fully-sampled, so-called "football region", so it is natural to define $\boldsymbol{G}$ to be a hypothetical system matrix having extra detector rows such that the entire reconstruction volume is contained in its corresponding football region[2]. In general, we define $\boldsymbol{G}$ to be some $N_g \times n_p$ system matrix corresponding to an "ideal", fully sampled geometry, for which $\boldsymbol{G}'\boldsymbol{G}$ is approximately shift-invariant. The matrix $\boldsymbol{G}$ has the same number of columns as $\boldsymbol{A}$ but has more rows ($N_g > n_d$); the rows of A are a subset of the rows of $\boldsymbol{G}$.

Second, we replace the usual diagonal matrix $\boldsymbol{D}[c_i]$ in (19) with $\boldsymbol{D}[c_i]\boldsymbol{P}$ where $\boldsymbol{P}$ is a $n_d \times N_g$ matrix that selects the rows of the hypothetical geometry $\boldsymbol{G}$ corresponding to those of the actual geometry $\boldsymbol{A}$. Each row of $\boldsymbol{P}$ is entirely zero except for a single element that is unity. By ordering the rows of $\boldsymbol{G}$ appropriately, we can use $\boldsymbol{P} = [\boldsymbol{I}_{n_d} \boldsymbol{0}_{n_d \times (N_g - n_d)}]$. An important property of the row selection matrix $\mathbf{P}$ is that $\boldsymbol{P}'\boldsymbol{W}\boldsymbol{P}$ is a $N_g \times N_g$ diagonal matrix where each diagonal element corresponds to a $w_i$ value for actual rays and is zero for the hypothetical rays.

With this generalization, we can rewrite the Fisher information matrix of the data fitting term as follows:

$$\boldsymbol{A}'\boldsymbol{W}\boldsymbol{A} = \boldsymbol{D}[s_j]\boldsymbol{G}'\boldsymbol{P}'\boldsymbol{D}[c_i]\boldsymbol{W}\boldsymbol{D}[c_i]\boldsymbol{P}\boldsymbol{G}\boldsymbol{D}[s_j] = \boldsymbol{D}[s_j]\boldsymbol{G}'\boldsymbol{P}'\boldsymbol{D}[W_i c_i^2]\boldsymbol{P}\boldsymbol{G}\boldsymbol{D}[s_j]. \quad (20)$$

Since the Fisher information matrix is fairly concentrated near its diagonal elements [1, Fig. 2], we approximate (20) as

$$\boldsymbol{A}'\boldsymbol{W}\boldsymbol{A} \approx \boldsymbol{D}[s_j]\boldsymbol{D}[\eta_j]\boldsymbol{G}'\boldsymbol{G}\boldsymbol{D}[\eta_j]\boldsymbol{D}[s_j] = \boldsymbol{D}[\lambda_j]\boldsymbol{G}'\boldsymbol{G}\boldsymbol{D}[\lambda_j] = \boldsymbol{\Lambda}\boldsymbol{G}'\boldsymbol{G}\boldsymbol{\Lambda}, \quad (21)$$

where the following factors match the diagonals of (21):

$$\eta_j = \sqrt{\frac{\sum_{i=1}^{n_d} g_{ij}^2 c_i^2 w_i}{\sum_{i=1}^{N_g} g_{ij}^2}}, \quad (22)$$

$$\lambda_j = s_j \eta_j = \sqrt{\frac{\sum_{i=1}^{n_d} a_{ij}^2 w_i}{\sum_{i=1}^{N_g} g_{ij}^2}}, \quad (23)$$

[2]A hypothetical parallel-beam geometry is another option for $\boldsymbol{G}$ that may lead to $\boldsymbol{G}'\boldsymbol{G}$ that is even more shift-invariant; that choice would require an additional cone-to-parallel rebinning process [30].

$$\boldsymbol{\Lambda} \triangleq \boldsymbol{D}[\lambda_j]. \quad (24)$$

Different choices of $c_i$ and $s_j$ will lead to various designs for $\boldsymbol{G} = \{g_{ij}\}$. As an example, for axial cone-beam CT, assuming $c_i = 1, \forall i$, and $s_j = 1, \forall j$, will lead to $\boldsymbol{G}$ that corresponds to another axial cone-beam CT geometry with extended detector rows and full 360 degree orbit. For some other choices, we may not have a physical interpretation for the system represented by $\boldsymbol{G}$.

Both the ray- and voxel-dependent factors need to be designed based on the modality, *i.e.*, for SPECT, $s_j$ should be designed to properly model the nonuniform spatial sensitivity and, for PET, $c_i$ should represent detector characteristics.

### B. Regularization with Uniform Resolution Property

Substituting (21) into (9) yields the following approximation for the local impulse response at the $j$th voxel:

$$\boldsymbol{l}_j \approx \left(\boldsymbol{\Lambda}\boldsymbol{G}'\boldsymbol{G}\boldsymbol{\Lambda}+\boldsymbol{R}\right)^{-1}\boldsymbol{\Lambda}\boldsymbol{G}'\boldsymbol{G}\boldsymbol{\Lambda}\boldsymbol{\delta}_j=\boldsymbol{\Lambda}^{-1}\left(\boldsymbol{G}'\boldsymbol{G}+\boldsymbol{\Lambda}^{-1}\boldsymbol{R}\boldsymbol{\Lambda}^{-1}\right)^{-1}\boldsymbol{G}'\boldsymbol{G}\boldsymbol{\Lambda}\boldsymbol{\delta}_j. \quad (25)$$

Typically, the local impulse response $\boldsymbol{l}_j$ is concentrated about voxel $j$ and clearly $\boldsymbol{\Lambda}\boldsymbol{\delta}_j = \lambda_j\boldsymbol{\delta}_j$. Following [1, eqn. (34)], we approximate (25) as the following final expression for the local impulse response:

$$\boldsymbol{l}_j \approx \left(\boldsymbol{G}'\boldsymbol{G}+\lambda_j^{-2}\boldsymbol{R}\right)^{-1}\boldsymbol{G}'\boldsymbol{G}\boldsymbol{\delta}_j. \quad (26)$$

Having analyzed the local impulse response, we focus on designing the coefficients $\{\kappa_j\}$ in the regularizer (5); these coefficients affect the Hessian $\boldsymbol{R}$ in (26) and thus control the spatial resolution. Our goal here is to choose $\{\kappa_j\}$ to provide approximately uniform spatial resolution by matching the local impulse response at the $j$th voxel, $\boldsymbol{l}_j$, to a target local impulse response, $\boldsymbol{l}_{\text{ref}}$, *i.e.*, $\boldsymbol{l}_j \approx \boldsymbol{l}_{\text{ref}}$. Using (26), we write the target local impulse response at a reference point, such as the isocenter, as follows:

$$\boldsymbol{l}_{\text{ref}} \triangleq \left(\boldsymbol{G}'\boldsymbol{G}+\boldsymbol{R}_0\right)^{-1}\boldsymbol{G}'\boldsymbol{G}\boldsymbol{\delta}_{\text{ref}}, \quad (27)$$

where $\boldsymbol{R}_0$ is the Hessian of a regularizer $\mathrm{R}_0(\boldsymbol{x})$ that provides desirable spatial resolution properties at the reference point. $\mathrm{R}_0(\boldsymbol{x})$ has the same form as (5) but possibly with a different set of $\{\kappa_j\}$ values, *e.g.*, $\kappa_j = 1, \forall j$.

Our design for $\boldsymbol{G}$ leads to $\boldsymbol{G}'\boldsymbol{G}\boldsymbol{\delta}_j$ being approximately locally shift invariant, and we assume $\boldsymbol{R}\boldsymbol{\delta}_j$ is also approximately locally shift-invariant [10, eqn. (15)]. Taking the Fourier transform of (26) yields the following expression for the local frequency response

$$L^j \approx \frac{F(\boldsymbol{G}'\boldsymbol{G}\boldsymbol{\delta}_j)}{F(\boldsymbol{G}'\boldsymbol{G}\boldsymbol{\delta}_j)+\lambda_j^{-2}F(\boldsymbol{R}\boldsymbol{\delta}_j)}, \quad (28)$$

where $F(\cdot)$ denotes 3-D DFT centered at voxel $j$. We want to match the local frequency response of $j$th voxel to the target frequency response, *i.e.*,

$$L^j \approx \frac{F(\boldsymbol{G}'\boldsymbol{G}\boldsymbol{\delta}_j)}{F(\boldsymbol{G}'\boldsymbol{G}\boldsymbol{\delta}_j)+\lambda_j^{-2}F(\boldsymbol{R}\boldsymbol{\delta}_j)} \approx \frac{F(\boldsymbol{G}'\boldsymbol{G}\boldsymbol{\delta}_{\mathrm{ref}})}{F(\boldsymbol{G}'\boldsymbol{G}\boldsymbol{\delta}_{\mathrm{ref}})+F(\boldsymbol{R}_0\boldsymbol{\delta}_{\mathrm{ref}})} \approx L^{\mathrm{ref}}. \quad (29)$$

Cross multiplying and simplifying yields

$$F(\boldsymbol{R}\boldsymbol{\delta}_j)F(\boldsymbol{G}'\boldsymbol{G}\boldsymbol{\delta}_{\mathrm{ref}}) \approx \lambda_j^2 F(\boldsymbol{R}_0\boldsymbol{\delta}_{\mathrm{ref}})F(\boldsymbol{G}'\boldsymbol{G}\boldsymbol{\delta}_j). \quad (30)$$

We design $\{\kappa_j\}$ by minimizing the least squares difference between both sides of (30)

$$\hat{\kappa}_j = \underset{\kappa_j \in \mathbb{R}_+}{\arg\min} \left\| F(\boldsymbol{R}\boldsymbol{\delta}_j)F(\boldsymbol{G}'\boldsymbol{G}\boldsymbol{\delta}_{\mathrm{ref}}) - \lambda_j^2 F(\boldsymbol{R}_0\boldsymbol{\delta}_{\mathrm{ref}})F(\boldsymbol{G}'\boldsymbol{G}\boldsymbol{\delta}_j) \right\|^2,$$

where $\mathbb{R}_+$ denotes nonnegative reals. For the quadratic potential function, the local frequency response of the regularizer Hessian is [16, eqn. (16)]

$$F(\boldsymbol{R}\boldsymbol{\delta}_j) = \kappa_j^2 R_\omega, \quad (32)$$

$$R_\omega \triangleq \sum_{l=1}^{N_l} \beta_l \left| C_l(\omega_1, \omega_2, \omega_3) \right|^2, \quad (33)$$

using the usual approximation $\kappa_j \approx \kappa_l$ for $l$ within the neighborhood of $j$, where $C_l$ denotes the discrete-space Fourier transform of $C_l[n, m, z]$ and $\omega$ denotes the digital frequency. Without loss of generality, we choose $R_0(\boldsymbol{x})$ such that

$$F(\boldsymbol{R}_0\boldsymbol{\delta}_{\mathrm{ref}}) = \sum_{l=1}^{N_l} \beta_l \left| C_l(\omega_1, \omega_2, \omega_3) \right|^2 = R_\omega. \quad (34)$$

Substituting (32) and (34) into (31) yields the following simplified expression:

$$\hat{\kappa}_j = \underset{\kappa_j \in \mathbb{R}_+}{\arg\min} \left\| \kappa_j^2 R_\omega F(\boldsymbol{G}'\boldsymbol{G}\boldsymbol{\delta}_{\mathrm{ref}}) - \lambda_j^2 R_\omega F(\boldsymbol{G}'\boldsymbol{G}\boldsymbol{\delta}_j) \right\|^2. \quad (35)$$

Solving (35), we obtain

$$\hat{\kappa}_j = \lambda_j \frac{\sqrt{\Re_+(\langle R_\omega F(\boldsymbol{G}'\boldsymbol{G}\boldsymbol{\delta}_{\mathrm{ref}}), R_\omega F(\boldsymbol{G}'\boldsymbol{G}\boldsymbol{\delta}_j)\rangle)}}{\|R_\omega F(\boldsymbol{G}'\boldsymbol{G}\boldsymbol{\delta}_{\mathrm{ref}})\|}, \quad (36)$$

where $\langle \cdot, \cdot \rangle$ denotes the inner product for 3D DFT space, and $\Re_+(\cdot)$ denotes the nonnegative real part.

When $\boldsymbol{G}'\boldsymbol{G}$ is approximately shift-invariant, we have

$$F(\boldsymbol{G}'\boldsymbol{G}\boldsymbol{\delta}_j) \approx F(\boldsymbol{G}'\boldsymbol{G}\boldsymbol{\delta}_{\mathrm{ref}}), \quad (37)$$

and the ratio in (36) becomes unity and (36) simplifies to $\hat{\kappa_j} = \lambda_j$.

The presented design process can address more general purposes besides obtaining resolution uniformity. For instance, one may want to match a spatially varying target response that depends on certain characteristics, such as the sampling at each voxel, so that each voxel would have different resolution properties for specific purposes.

Our new regularizer for uniform resolution properties in the reconstructed image (hereafter R-REG) is given by (5) with

$$\hat{\kappa}_j = \lambda_j = \sqrt{\frac{\sum_{i=1}^{n_\mathrm{d}} a_{ij}^2 w_i}{\sum_{i=1}^{N_\mathrm{g}} g_{ij}^2}}. \quad (38)$$

This new pre-tuned spatial strength function (38) has a very similar form to that of the original certainty (6) proposed in [1], but with a different denominator. This new denominator takes effect when voxel $j$ is at an undersampled location. When it is fully-sampled, the new pre-tuned spatial strength is exactly the same as the original certainty since $\sum_{i=1}^{N_\mathrm{g}} g_{ij}^2 = \sum_{i=1}^{n_\mathrm{d}} a_{ij}^2$ for such locations. For undersampled region, this new denominator decreases the regularization strength, leading to sharper and possibly noisier reconstructed images compared to using the original aggregated certainty (6).

To simplify implementation, we approximate (38) as follows

$$\hat{\kappa}_j \approx \sqrt{\frac{\sum_{i=1}^{n_\mathrm{d}} a_{ij} w_i}{\sum_{i=1}^{N_\mathrm{g}} g_{ij}}}. \quad (39)$$

Unlike the back-projection of the statistical weighting, $\sum_{i=1}^{n_\mathrm{d}} a_{ij} w_i$, calculating the sum of rows of the Hessian $\boldsymbol{A}'\boldsymbol{W}\boldsymbol{A}$, $\sum_{i=1}^{n_\mathrm{d}} a_{ij}^2 w_i$, is sometimes not available or easily implementable. Empirical results in the supplement verify that (39) closely approximates (38).

Even though the new regularizer design was derived for quadratic regularization, it can be also applied to regularizes with non-quadratic potential functions, following the spirit of [31]. Of course edge-preserving regularization always leads to non-uniform spatial resolution near image edges, and this important characteristic will be retained.

The proposed regularizer (38) attempts to address non-uniformities caused by both shift-variant scanning geometries and by interactions between the regularization and the statistical weights. The derivation assumed that $\kappa_j$ changes very slowly within its neighborhood. However, this assumption may fail for certain regions such as near the edges of a structure. Furthermore, since we are only adjusting the "overall strength" of the regularization at each voxel and not its "directional strength" for each neighboring voxel, the proposed regulariza tion cannot correct for asymmetry in local impulse responses. The proposed regularization is designed to generate uniform spatial resolution in terms of CRC. To obtain isotropic local impulse response, one would need to design the directional coefficients, $\beta_l$, at each location [17].

### C. Regularization with Uniform Noise Property

Using the Fisher information matrix approximation (21), we approximate the local noise correlation corr($\hat{\boldsymbol{x}}$) as follows

$$\operatorname{corr}(\hat{\boldsymbol{x}}_j) \approx (\overline{\boldsymbol{\Lambda}}\boldsymbol{G}'\boldsymbol{G}\overline{\boldsymbol{\Lambda}}+\boldsymbol{R})^{-1}\hat{\boldsymbol{\Lambda}}\boldsymbol{G}'\boldsymbol{G}\hat{\boldsymbol{\Lambda}}(\overline{\boldsymbol{\Lambda}}\boldsymbol{G}'\boldsymbol{G}\overline{\boldsymbol{\Lambda}}+\boldsymbol{R})^{-1}\boldsymbol{\delta}_j, \quad (40)$$

where, using $v_i$ and $\hat{w}_i$ from (14):

$$\overline{\lambda}_j \triangleq \sqrt{\frac{\sum_{i=1}^{n_\mathrm{d}} a_{ij}^2 \hat{w}_i v_i}{\sum_{i=1}^{N_\mathrm{g}} g_{ij}^2}}, \overline{\boldsymbol{\Lambda}} \triangleq \boldsymbol{D}[\overline{\lambda}_j], \quad (41)$$

$$\hat{\lambda}_j \triangleq \sqrt{\frac{\sum_{i=1}^{n_\mathrm{d}} a_{ij}^2 \hat{w}_i v_i^2}{\sum_{i=1}^{N_\mathrm{g}} g_{ij}^2}}, \hat{\boldsymbol{\Lambda}} \triangleq \boldsymbol{D}[\hat{\lambda}_j]. \quad (42)$$

We further approximate (40) as

$$\operatorname{corr}(\hat{\boldsymbol{x}}_j) \approx \overline{\boldsymbol{\Lambda}}^{-1}(\boldsymbol{G}'\boldsymbol{G}+\overline{\boldsymbol{\Lambda}}^{-1}\boldsymbol{R}\overline{\boldsymbol{\Lambda}}^{-1})^{-1-}\overline{\boldsymbol{\Lambda}}^{-1}\hat{\boldsymbol{\Lambda}}\boldsymbol{G}'\boldsymbol{G}\hat{\boldsymbol{\Lambda}}\overline{\boldsymbol{\Lambda}}^{-1}(\boldsymbol{G}'\boldsymbol{G}+\overline{\boldsymbol{\Lambda}}^{-1}\boldsymbol{R}\overline{\boldsymbol{\Lambda}}^{-1})^{-1}\overline{\boldsymbol{\Lambda}}^{-1}\boldsymbol{\delta}_j \approx \frac{\hat{\lambda}_j^2}{\overline{\lambda}_j^4}(\boldsymbol{G}'\boldsymbol{G}+\overline{\lambda}_j^{-2}\boldsymbol{R})^{-1}\boldsymbol{G}'\boldsymbol{G}(\boldsymbol{G}'\boldsymbol{G}+\overline{\lambda}_j^{-2}\boldsymbol{R})^{-}$$

using the usual assumption that the local noise correlation corr($\hat{\boldsymbol{x}}$) is concentrated about voxel $j$. From (43), the local noise power spectrum (NPS) of voxel $j$ is approximately

$$S^j \approx \frac{\hat{\lambda}_j^2}{\overline{\lambda}_j^4}\frac{F(\boldsymbol{G}'\boldsymbol{G}\boldsymbol{\delta}_j)}{(F(\boldsymbol{G}'\boldsymbol{G}\boldsymbol{\delta}_j)+\overline{\lambda}_j^{-2}F(\boldsymbol{R}\boldsymbol{\delta}_j))^2}. \quad (44)$$

To obtain uniform noise properties, we want to match the local NPS at the *j*th voxel to a target NPS, *i.e.*, $S^j \approx S^{\text{ref}}$. For the target, we use the local NPS at a reference point and assume that the regularizer $R_0(\boldsymbol{x})$ was chosen to provide a suitable NPS at that location. Our design goal becomes:

$$\frac{\hat{\lambda}_j^2}{\overline{\lambda}_j^4}\frac{F(\boldsymbol{G}'\boldsymbol{G}\boldsymbol{\delta}_j)}{\left(F(\boldsymbol{G}'\boldsymbol{G}\boldsymbol{\delta}_j)+\overline{\lambda}_j^{-2}F(\boldsymbol{R}\boldsymbol{\delta}_j)\right)^2} \approx \frac{\hat{\lambda}_{\text{ref}}^2}{\overline{\lambda}_{\text{ref}}^4}\frac{F(\boldsymbol{G}'\boldsymbol{G}\boldsymbol{\delta}_{\text{ref}})}{\left(F(\boldsymbol{G}'\boldsymbol{G}\boldsymbol{\delta}_{\text{ref}})+F(\boldsymbol{R}_0\boldsymbol{\delta}_{\text{ref}})\right)^2}. \quad (45)$$

Cross multiplying leads to

$$\hat{\lambda}_j^2\overline{\lambda}_{\text{ref}}^4 F(\boldsymbol{G}'\boldsymbol{G}\boldsymbol{\delta}_j)\left(F(\boldsymbol{G}'\boldsymbol{G}\boldsymbol{\delta}_{\text{ref}})+F(\boldsymbol{R}_0\boldsymbol{\delta}_{\text{ref}})\right)^2 \approx \hat{\lambda}_{\text{ref}}^2\overline{\lambda}_j^4 F(\boldsymbol{G}'\boldsymbol{G}\boldsymbol{\delta}_{\text{ref}})\left(F(\boldsymbol{G}'\boldsymbol{G}\boldsymbol{\delta}_j)+\overline{\lambda}_j^{-2}F(\boldsymbol{R}\boldsymbol{\delta}_j)\right)^2. \quad (46)$$

Using (32) and (34), we simplify (46) to

$$\kappa_j^2\sqrt{F(\boldsymbol{G}'\boldsymbol{G}\boldsymbol{\delta}_{\text{ref}})}R_\omega \approx \left(\frac{\hat{\lambda}_j\overline{\lambda}_{\text{ref}}^2}{\hat{\lambda}_{\text{ref}}}\right)\sqrt{F(\boldsymbol{G}'\boldsymbol{G}\boldsymbol{\delta}_j)}\left(F(\boldsymbol{G}'\boldsymbol{G}\boldsymbol{\delta}_{\text{ref}})+R_\omega\right)-\overline{\lambda}_j^2\sqrt{F(\boldsymbol{G}'\boldsymbol{G}\boldsymbol{\delta}_{\text{ref}})}F(\boldsymbol{G}'\boldsymbol{G}\boldsymbol{\delta}_j). \quad (47)$$

By defining $B_\omega^{\text{ref}} \triangleq F(\boldsymbol{G}'\boldsymbol{G}\boldsymbol{\delta}_{\text{ref}})$ and $B_\omega^j \triangleq F(\boldsymbol{G}'\boldsymbol{G}\boldsymbol{\delta}_j)$, can be rewritten as follows:

$$\kappa_j^2\sqrt{B_\omega^{\text{ref}}}R_\omega \approx \left(\frac{\hat{\lambda}_j\overline{\lambda}_{\text{ref}}^2}{\hat{\lambda}_{\text{ref}}}\right)\sqrt{B_\omega^j}\left(B_\omega^{\text{ref}}+\boldsymbol{R}_\omega\right)-\overline{\lambda}_j^2\sqrt{B_\omega^{\text{ref}}}B_\omega^j. \quad (48)$$

We design $\{\kappa_j\}$ by solving the following least squares problem

$$\hat{\kappa}_j=\underset{\kappa_j\in\mathbb{R}_+}{\arg\min}\left\|\kappa_j^2\sqrt{B_\omega^{\text{ref}}}R_\omega-\left[\left(\frac{\hat{\lambda}_j\overline{\lambda}_{\text{ref}}^2}{\hat{\lambda}_{\text{ref}}}\right)\sqrt{B_\omega^j}\left(B_\omega^{\text{ref}}+R_\omega\right)-\overline{\lambda}_j^2\sqrt{B_\omega^{\text{ref}}}B_\omega^j\right]\right\|^2. \quad (49)$$

The solution to (49) is given by

$$\hat{\kappa}_j=\frac{1}{\left\|\sqrt{B_\omega^{\text{ref}}}R_\omega\right\|}\left[\Re_+\left(\left(\frac{\hat{\lambda}_j\overline{\lambda}_{\text{ref}}^2}{\hat{\lambda}_{\text{ref}}}\right)\left\langle\sqrt{B_\omega^{\text{ref}}}R_\omega,\sqrt{B_\omega^j}R_\omega\right\rangle+\left(\frac{\hat{\lambda}_j\overline{\lambda}_{\text{ref}}^2}{\hat{\lambda}_{\text{ref}}}\right)\left\langle\sqrt{B_\omega^{\text{ref}}}R_\omega,\sqrt{B_\omega^j}B_\omega^{\text{ref}}\right\rangle-\overline{\lambda}_j^2\left\langle\sqrt{B_\omega^{\text{ref}}}R_\omega,\sqrt{B_\omega^{\text{ref}}}B_\omega^j\right\rangle\right)\right]^{\frac{1}{2}}. \quad (50)$$

Using (37), we simplify (50) as follows

$$\hat{\kappa}_j=\sqrt{\left(\frac{\overline{\lambda}_{\text{ref}}^2}{\hat{\lambda}_{\text{ref}}}\right)\hat{\lambda}_j+E_\omega\left[\left(\frac{\overline{\lambda}_{\text{ref}}^2}{\hat{\lambda}_{\text{ref}}}\right)\hat{\lambda}_j-\overline{\lambda}_j^2\right]}, \quad (51)$$

Where $E_\omega=\Re_+\left(\left\langle\sqrt{B_\omega^{\text{ref}}}R_\omega,\sqrt{B_\omega^{\text{ref}}}B_\omega^{\text{ref}}\right\rangle\right)/\left\|\sqrt{B_\omega^{\text{ref}}}R_\omega\right\|^2$.

Regularizer (5) with (51) (hereafter N-REG) provides approximately uniform noise properties in the reconstructed image. The new $\{\kappa_j\}$ factors (51) consist of two terms within a square root. If we ignore the second term, then (51) is approximately the square root of the modified pre-tuned spatial strength (38) of R-REG. This suggests that N-REG has decreased regularization strength at undersampled region compared to A-REG, but with less spatial variation than R-REG. The second term of (51) is an "adjustment" that is usually smaller than the first term.

## IV. Results

This section investigates the effect of the proposed regularizers (see Table I for acronyms) for PWLS image reconstruction of 3D short-scan axial CT using both phantom and clinical data. For the hypothetical geometry $G$, we assumed $c_i = 1, \forall i$, and $s_j = 1, \forall j$, in (20) and used a full 360° scan with increased number of detector rows, $N_{\mathrm{t}}^{\mathrm{ext}}$ (see the supplement for a different choice of $\boldsymbol{G}$).

### A. Resolution Uniformity

**1) Phantom Simulation—**An anthropomorphic phantom simulation was used to demonstrate the improved spatial resolution uniformity induced by the regularizer with the modified pre-tuned spatial strength (38). We used 512 × 512 × 122 XCAT phantom [32] with voxel size $\Delta_{\mathrm{x}} = \Delta_{\mathrm{y}} = 0.9766$ mm and $\Delta_{\mathrm{z}} = 0.625$ mm as our true image, $\boldsymbol{x}^{\mathrm{true}}$ (Fig. 1).

We used the separable footprint projector [33] to simulate a monoenergetic, noiseless sinogram for a 3rd-generation axial cone-beam CT system having $N_{\mathrm{s}} = 888$ channels and $N_{\mathrm{t}} = 64$ detector rows with spacings $\Delta_{\mathrm{s}} = 1.0239$ mm and $\Delta_{\mathrm{t}} = 1.09878$ mm. We assumed a short-scan protocol that covers an angular range of 227.6° with $N_{\mathrm{a}} = 622$ evenly spaced views. We selected the hypothetical geometry $\boldsymbol{G}$ to have both extended views, $N_{\mathrm{a}}^{\mathrm{ext}}=984$ over 360°, and detector rows, $N_{\mathrm{t}}^{\mathrm{ext}}=168$. The statistical weights were $w_i = b_0 \exp(-[\boldsymbol{Ax}]_i)$ where the X-ray intensity was $b_0 = 10^6$.

To obtain local impulse responses at various locations, we added impulses with amplitude $\varepsilon = 2.5 \times 10^{-4}$ mm$^{-1}$, corresponding to approximately 14 HU, to 6 different locations in each of the selected 9 slices (see Fig. 1 for impulse locations in xy plane). Selected slices were evenly spaced through z-dimension including isoplane, end slices of region-of-interest (ROI), and slices outside ROI. Axial ROI was selected as 5th to 60th slices (out of 64) to focus on slices with less short-scan artifacts due to insufficient sampling [34]. We used (8) to evaluate the local impulse response at each location for regularizer designs with both the original aggregated certainty (6) (hereafter A-REG) and the modified pre-tuned spatial strength function (38) (R-REG). Both quadratic and edge-preserving regularizations were investigated to show that the proposed regularizer design R-REG is applicable to both cases. Image reconstruction was done on the same grid as the true image. For this experiment, we set the regularization parameter A $\beta_l$ as $\beta_l = \beta, \forall l$, where $\beta$ was selected based on the full-width at half-maximum (FWHM) of the local impulse response at the isocenter. To visualize the shape of the local impulse response more clearly, we selected a somewhat large $\beta$ value for which the FWHM was approximately 3 times the voxel size. Image reconstruction used

the ordered-subsets with double surrogates (OSDS) method [35]. The number of iterations was 20 with 41 subsets.

First, we present the results for regularization with a quadratic potential function. Fig. 2 illustrates that the proposed regularizer (38) leads to local impulse response functions having more uniform CRC values than the "conventional" aggregated certainty design (6), particularly for off-center slices. CRC values of local impulse responses at different locations become nonuniform when using A-REG (6). This nonuniformity becomes severe as we move away from center slices. Using the proposed regularizer R-REG (38), the CRC values become much more uniform regardless of the location or the amount of sampling. R-REG (38) corrects only the nonuniformity of peak values of local impulse responses. Anisotropy in the shape of the impulse response could be improved by designing directional coefficients [17].

Fig. 3 shows *x* profiles through the center of all local impulse responses to compare CRC values more closely. Using A-REG (6) leads to resolution nonuniformity even in the center slice, primarily due to short-scan geometry. Nonuniformity in resolution becomes most severe for locations 2 to 4 that have much worse sampling compared to the isocenter due to the axial cone-beam geometry and the short-scan orbit.

Table II compares the average "mismatch" of the CRC values for the given 6 locations across slices and within each slice. We used the following definition of CRC mismatch

$$\rho_j \triangleq |\mathrm{CRC}(\boldsymbol{l}_j) - \mathrm{CRC}(\boldsymbol{l}_{\mathrm{ref}})| / |\mathrm{CRC}(\boldsymbol{l}_{\mathrm{ref}})|. \quad (52)$$

The proposed regularizer R-REG improved the uniformity of CRC values throughout the reconstruction volume. The average CRC mismatch was significantly improved for all locations and slices, and undersampled voxels were most improved by the proposed regularizer, as designed. The overall improvement of CRC mismatch was from 34.5% to 9.9%.

We obtained similar results for edge-preserving regularization with a hyperbola potential function [36] given by

$$\phi(t) = \delta^2 \left[ \sqrt{1 + |t/\delta|^2} - 1 \right]. \quad (53)$$

Shape of the local impulse responses does not change much compared to the quadratic regularization, but CRC values become slightly higher. As in the quadratic case, the original certainty function (6) yields non-uniform CRC values across multiple voxel locations, and proposed regularization (38) leads to more uniform CRC values. Due to their similarity to the quadratic case, results for edge-preserving regularization are presented in the supplementary material.

Even though proposed designs were based on approximations, such as (26), the local impulse response calculated by (8) yields CRC values that closely match the target CRC.

For both quadratic and edge-preserving regularizers, the proposed designs provide improved CRC uniformity (see also Table II).

**2) Real Clinical Data—**We reconstructed a clinical cardiac CT scan as a 1024 × 1024 × 122 image with 70 cm field-of-view (FOV). Measurements were obtained from a 64 row axial CT scanner with a short-scan protocol and 480 mAs tube current. The sinogram dimension was $[N_s, N_t, N_a] = [888, 64, 642]$. We selected the hypothetical geometry $\boldsymbol{G}$ to have both extended views, $N_{\mathrm{a}}^{\mathrm{ext}}=984$ and detector rows, $N_{\mathrm{t}}^{\mathrm{ext}}=148$. For this experiment, we set $\beta_l$ in (5) using [28]. We used ICD with spatially non-homogeneous updates [37] for reconstruction. We show results from both quadratic and edge-preserving regularization using the q-generalized Gaussian potential function with $p = 2$, $q = 1.2$, and $c = 10$, [3]

$$\phi(t)=\frac{|t|^p}{1+|t/c|^{p-q}}. \quad (54)$$

Fig. 4 compares the reconstructed images with a quadratic potential function and the following different regularizers: Uniform, A-REG, and R-REG When uniform regularization is used, *i.e.*, $\kappa_j = 1, \forall_j$, the reconstructed image becomes over-smoothed even for some locations in the center slice, illustrating the importance of the pre-tuned spatial strength function in the regularization. Reconstructed image using A-REG (6) shows less blurring and sharper spatial resolution compared to that of the uniform regularizer. However, even in the center slice, both left and right sides of the reconstructed image have different resolution. This is consistent with the result in Fig. 3 (a) where the CRC values were nonuniform even in the center slice due to short-scan orbit. The proposed regularizer R-REG (38) improved resolution uniformity in the center slice. In the end slices of the ROI, the resolution nonuniformity becomes more apparent. A-REG (6) fails to provide resolution uniformity at under-sampled locations, leading to visible differences in smoothness between left and right side of the reconstructed images. On the other hand, the reconstucted image using R-REG (38) has more uniform resolution properties even in these undersampled region, causing the structures in the region to have sharper boundaries.

Fig. 6 and Fig. 7 show reconstructed images for edge-preserving regularization. Clearly, the edge-preserving regularization preserves fine structures, leading to better image quality in terms of spatial resolution compared to the quadratic regularization. However, the choice of $\{\kappa_j\}$ still affects the resolution uniformity in the reconstructed image. The results show similar tendencies as in the quadratic case: non-uniform resolution and over-regularization in the undersampled region for uniform regularizer and A-REG. On the other hand, the proposed R-REG achieves sharper and more uniform spatial resolution. This suggests that even though the proposed regularizer was derived for a quadratic regularization, it is also suitable for non-quadratic regularization.

## B. Noise Uniformity

Reconstructed images using R-REG (38) have better resolution uniformity throughout the entire volume, however, this improvement comes at the expense of the noise properties. As shown in Fig. 7, the proposed R-REG slightly increases the noise level in the reconstructed

image when edge-preserving regularization is used. This trade-off is inevitable; thus we also investigated a regularizer that focuses on noise uniformity (N-REG, (51)).

**1) Phantom Experiment—**To compare the regularizes quantitativly, we used the GE performance phantom (GEPP) [20]. The phantom consists of a Plexiglas™ insert with resolution bars, and tungsten wires in water. The phantom was scanned with a 64 row axial CT scanner in short-scan mode and 70 mAs tube current, corresponding to a very low dose scan, and reconstructed to a grid of 1024 × 1024 × 90 with the following voxel size: $\Delta_x = \Delta_y = 0.2246$ mm and $\Delta_z = 0.625$. We selected the hypothetical geometry G to have both extended views, $N_{\mathrm{a}}^{\mathrm{ext}}=984$, and detector rows, $N_{\mathrm{t}}^{\mathrm{ext}}=200$. Edge-preserving regularization with q-generalized Gaussian potential function (54) was used.

Fig. 8 shows the reconstructed image of the GEPP with A-REG. Due to small FOV (= 23 cm), the end slices of the ROI did not suffer much from under-sampling. However, the choice of regularization still leads to different image qualities in the reconstructed images even in the center slice. To compare different regularizations fairly, we chose the regularization parameter $\beta$ such that the noise standard deviation near the isocenter is similar for all reconstructed images ($\approx$ 13.7 HU). We selected 7 different homogeneous regions in the center slice to compare the noise standard deviation (see Fig. 8 for their locations). Table III illustrates that the proposed N-REG shows the best noise uniformity, *i.e.*, the average standard deviation of the noise is reasonably close to that of the region near the isocenter. Since the FOV is small, the noise standard deviation does not vary much within the Plexiglas™ insert. However, the standard deviation in the wall depends significantly on the regularization method. Due to the symmetrical shape of the GEPP and thickness of its wall, the statistical weighting varies mostly only in the channel dimension (except for the views affected by an additional weighting such as Parker weighting) and is “U” shaped. As a result, the uniform regularizer generally increased noise in the reconstructed image, and both A-REG and R-REG over-regularized the region far away from the isocenter, *i.e.*, the walls in this case. Both A-REG and R-REG showed similar performance as expected, and N-REG improved noise uniformity in the reconstructed image.

**2) Real Clinical Data—**Fig. 4 to Fig. 7 compare the reconstructed images obtained using various regularizers. For both quadratic and edge-preserving regularizers, the proposed N-REG provides improved noise uniformity in the reconstructed image. The uniform regularizer tends to over-smooth the reconstructed image, and A-REG shows nonuniform noise properties even in the center slice. Both proposed R-REG and N-REG show improved image qualities in terms of resolution and noise, respectively. R-REG shows somewhat sharper reconstructed image compared to N-REG on end slices for both regularizers, but has slightly higher and nonuniform noise variance.

Fig. 5 and Fig. 7 zoom into the reconstructed images at the last slice of ROI, which has nonuniform sampling over the slice. A reconstructed image from full scan measurements with A-REG was used as a reference with desirable image quality. Since the image quality of the reference image is also affected by the choice of regularization, it may not be the optimal image for clinical diagnosis. However, the under-sampling from short-scan measurements is a more dominant factor for the image quality in the displayed region, so the

chosen reference image shows better image characteristics compared to the other reconstructed images from short-scan measurements. For each case, the region on the right side of the reconstructed image (bottom row) was compared to the left side of the image that has less sampling (top row). Uniform regularization clearly leads to over-regularization in the undersampled region, causing severe noise nonuniformity within the slice. Even though less severe, A-REG also suffers from the same issue. Proposed regularization N-REG generated a reconstructed image with better noise uniformity, improving visibility of structures in the undersampled region.

For both examples, the proposed N-REG (51) provides more uniform noise characteristics in the reconstructed image compared to other regularization methods.

## V. Discussion

We proposed new regularization methods by modifying the aggregated certainty presented in [1] using the hypothetical geometry concept. Proposed regularizer R-REG in (38) improved the spatial resolution uniformity in the reconstructed images, and N-REG in (51) provided more uniform noise characteristics compared to the uniform and aggregated certainty regularizers.

The proposed methods, R-REG and N-REG, showed improved spatial resolution or noise uniformity compared to the conventional uniform regularizer and A-REG in both quadratic and edge-preserving regularizations and for both simulated and clinical scans. Even though the proposed regularizers were targeted to improve the uniformity of either the spatial resolution or noise, they yielded reconstructed images with qualitatively improved image quality in terms of resolution or noise compared to that from the uniform and the aggregated certainty regularizers. For quadratic regularization, the noise characteristics have less effect on the visual image quality than the spatial resolution, suggesting the use of R-REG to improve spatial resolution uniformity. On the other hand, since edge-preserving regularization provides improved resolution near edges, the noise uniformity primarily affects the readability of the reconstructed image. Thus, N-REG may be preferable for edge-preserving regularization. However, there are tradeoffs between spatial resolution and noise characteristics. Using either regularizer may not provide an optimal reconstructed image in terms of both resolution and noise. Furthermore, it is unknown which feature is more desirable for diagnosis. Diagnostic readability for the reconstructed images obtained from both methods needs to be investigated to determine the best regularizer, and possibly some combination of methods may be desirable. A compromise approach that balances spatial resolution and noise characteristics is explored in the supplement as a starting point for further research.

For experiments in this paper, we used the hypothetical scanning geometry obtained intuitively by extending both rows and views from given axial cone-beam CT geometry. Another option would be to use a step-and-shoot set of axial scans. For some other geometries, determining the appropriate hypothetical geometry may be harder. For example, in helical CT, simply extending views would not suffice, and since the actual scanning geometry must be a subset of the hypothetical geometry, we cannot use a very small pitch

for $\boldsymbol{G}$. Multiple intertwined helical geometries is a possible choice. Careful consideration is required to properly extend the proposed regularization designs to other scanning geometries.

One minor drawback of using the generalized geometry is the increased computation for (23). For a geometry having extended views or rows, since (23) is calculated only once prior to iterating, the increased computation is insignificant compared to the computation required for the actual reconstruction. However, using a step-and-shoot set of axial scans or intertwined multiple helical scans may require considerable computations. Fortunately, since calculating (23) only requires the hypothetical geometry, one could tabulate the denominator of (23).

The proposed regularizers improve the uniformity of spatial resolution or noise by controlling a scaling factor at each voxel. Even though the design process attempts to match the entire local impulse responses or NPS functions, they are primarily matching CRC values and variances at each location due to approximations (26) and (43). Thus, the proposed regularizers do not correct anisotropy of these characteristics. Designing directional coefficients in the regularizer may correct for such anisotropy, and has shown promising results for the well-sampled regions [16], [18]. However, the anisotropy of the image characteristics in the under-sampled region is hard to correct, especially since these methods use locally circulant approximations of the Fisher information matrix. One possible future work is to extend the methods in this paper to directional coefficient design.

## Supplementary Material

Refer to Web version on PubMed Central for supplementary material.

## Acknowledgments

The authors would like to thank J. B. Thibault and De-bashish Pal for providing the scan data and valuable comments. The authors also thank K. Sauer and C. Bouman for discussions of CT noise statistics and regularization design.

This work was supported in part by GE Healthcare and CPU donation from Intel Corporation.

## References

1. Fessler JA, Rogers WL. Spatial resolution properties of penalized-likelihood image reconstruction methods: Space-invariant tomographs. IEEE Trans Im Proc. Sep; 1996 5(9):1346–58.
2. Fessler, JA. Statistical image reconstruction methods for transmission tomography. In: Sonka, M.; Fitzpatrick, JM., editors. Handbook of Medical Imaging, Volume 2 Medical Image Processing and Analysis. Bellingham: SPIE; 2000. p. 1-70.
3. Thibault JB, Sauer K, Bouman C, Hsieh J. A three-dimensional statistical approach to improved image quality for multi-slice helical CT. Med Phys. Nov; 2007 34(11):4526–44. [PubMed: 18072519]
4. Qi J, Huesman RH. Theoretical study of lesion detectability of MAP reconstruction using computer observers. IEEE Trans Med Imag. Aug; 2001 20(8):815–22.
5. Chatziioannou A, Qi J, Annala A, Moore A, Leahy RM, Cherry SR. Comparison of 3D MAP and FBP algorithms for image reconstruction in microPET. IEEE Trans Med Imag. May; 2000 19(5): 507–12.

6. Imai K, Ikeda M, Enchi Y, Niimi T. Statistical characteristics of streak artifacts on CT images: Relationship between streak artifacts and mA s values. Med Phys. Feb; 2009 36(2):492–9. [PubMed: 19291988]
7. Orlov SS. Theory of three dimensional reconstruction. I. Conditions for a complete set of projections. Sov Phys Crystallography. 1976; 20:312–14.
8. Tuy HK. An inversion formula for cone-beam reconstruction. SIAM J Appl Math. Jun; 1983 43(3): 546–52.
9. Qi J, Leahy RM. A theoretical study of the contrast recovery and variance of MAP reconstructions from PET data. IEEE Trans Med Imag. Apr; 1999 18(4):293–305.
10. Qi J, Leahy RM. Resolution and noise properties of MAP reconstruction for fully 3D PET. IEEE Trans Med Imag. May; 2000 19(5):493–506.
11. Nuyts J, Fessler JA. A penalized-likelihood image reconstruction method for emission tomography, compared to post-smoothed maximum-likelihood with matched spatial resolution. IEEE Trans Med Imag. Sep; 2003 22(9):1042–52.
12. Mustafovic S, Thielemans K. Object dependency of resolution in reconstruction algorithms with inter-iteration filtering applied to PET data. IEEE Trans Med Imag. Apr; 2004 23(4):433–46.
13. Ramani S, Fessler JA. A splitting-based iterative algorithm for accelerated statistical X-ray CT reconstruction. IEEE Trans Med Imag. Mar; 2012 31(3):677–88.
14. Jian YT, Carson RE. Feasible uniform-resolution penalized likelihood reconstruction for static- and multi-frame 3D PET. Proc IEEE Nuc Sci Symp Med Im Conf. 2013
15. Stayman JW, Fessler JA. Regularization for uniform spatial resolution properties in penalized-likelihood image reconstruction. IEEE Trans Med Imag. Jun; 2000 19(6):601–15.
16. Shi HR, Fessler JA. Quadratic regularization design for 2D CT. IEEE Trans Med Imag. May; 2009 28(5):645–56.
17. Cho JH, Fessler JA. Quadratic regularization design for 3d axial Ct. Proc Intl Mtg on Fully 3D Image Recon in Rad and Nuc Med. 2013:78–81.
18. Cho JH, Fessler JA. Quadratic regularization design for 3D axial Ct: Towards isotropic noise. Proc IEEE Nuc Sci Symp Med Im Conf. 2013
19. Sauer K, Bouman C, Thibault JB. Noise modeling for model-based image reconstruction in X-ray CT. 2014 preprint.
20. Hsieh, J. Computed tomography: Principles, design, artifacts, and recent advances. Bellingham: SPIE; 2003.
21. Whiting BR, Massoumzadeh P, Earl OA, O'Sullivan JA, Snyder DL, Williamson JF. Properties of preprocessed sinogram data in x-ray computed tomography. Med Phys. Sep; 2006 33(9):3290–303. [PubMed: 17022224]
22. Nuyts J, De Man B, Fessler JA, Zbijewski W, Beekman FJ. Modelling the physics in iterative reconstruction for transmission computed tomography. Phys Med Biol. Jun; 2013 58(12):R63–96. [PubMed: 23739261]
23. La Riviere PJ, Bian J, Vargas PA. Penalized-likelihood sinogram restoration for computed tomography. IEEE Trans Med Imag. Aug; 2006 25(8):1022–36.
24. Fessler JA. Hybrid Poisson/polynomial objective functions for tomographic image reconstruction from transmission scans. IEEE Trans Im Proc. Oct; 1995 4(10):1439–50.
25. Sauer K, Bouman C. A local update strategy for iterative reconstruction from projections. IEEE Trans Sig Proc. Feb; 1993 41(2):534–48.
26. Fessler JA. Mean and variance of implicitly defined biased estimators (such as penalized maximum likelihood): Applications to tomography. IEEE Trans Im Proc. Mar; 1996 5(3):493–506.
27. Stayman JW, Fessler JA. Compensation for nonuniform resolution using penalized-likelihood reconstruction in space-variant imaging systems. IEEE Trans Med Imag. Mar; 2004 23(3):269–84.
28. Yu Z, Bouman CA, Thibault JB, Sauer KD. Image grid invariant regularization for iterative reconstruction. Proc Intl Mtg on Fully 3D Image Recon in Rad and Nuc Med. 2013:517–20.
29. Parker DL. Optimal short scan convolution reconstruction for fan beam CT. Med Phys. Mar; 1982 9(2):254–7. [PubMed: 7087912]

30. Kachelrieß M, Schaller S, Kalender WA. Advanced single-slice rebinning in cone-beam spiral CT. Med Phys. Apr; 2000 27(4):754–72. [PubMed: 10798698]

31. Ahn S, Leahy RM. Analysis of resolution and noise properties of nonquadratically regularized image reconstruction methods for PET. IEEE Trans Med Imag. Mar; 2008 27(3):413–24.

32. Segars WP, Mahesh M, Beck TJ, Frey EC, Tsui BMW. Realistic CT simulation using the 4D XCAT phantom. Med Phys. Aug; 2008 35(8):3800–8. [PubMed: 18777939]

33. Long Y, Fessler JA, Balter JM. 3D forward and back-projection for X-ray CT using separable footprints. IEEE Trans Med Imag. Nov; 2010 29(11):1839–50.

34. Cho, JH. Ph D dissertation. Univ. of Michigan; Ann Arbor, MI: 2014. Improving statistical image reconstruction for cardiac X-ray computed tomography; p. 48109-2122.Ann Arbor, MI

35. Cho JH, Fessler JA. Accelerating ordered-subsets image reconstruction for X-ray CT using double surrogates. Proc SPIE Medical Imaging 2012: Phys Med Im. 2012:83131X.

36. Panin VY, Zeng GL, Gullberg GT. Total variation regulated EM algorithm. IEEE Trans Nuc Sci. Dec; 1999 46(6):2202–10.

37. Yu Z, Thibault JB, Bouman CA, Sauer KD, Hsieh J. Fast model-based X-ray CT reconstruction using spatially non-homogeneous ICD optimization. IEEE Trans Im Proc. Jan; 2011 20(1):161–75.

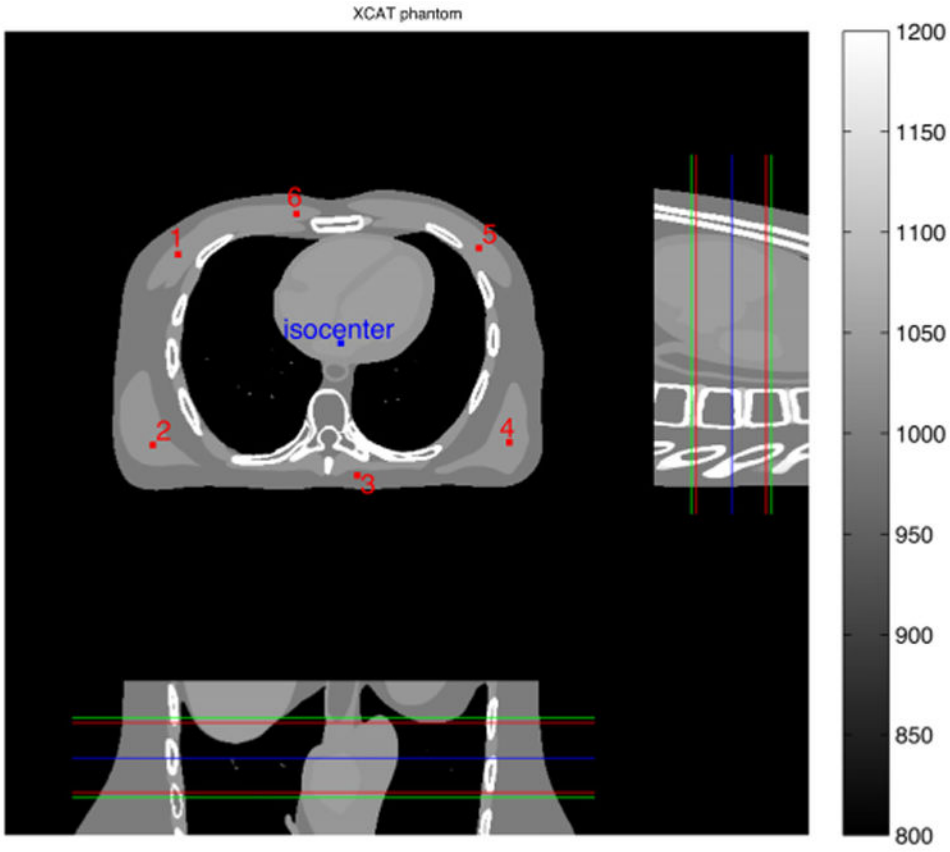


**Fig. 1.**

XCAT phantom used in the simulation. Middle 3 planes (*xy*, *xz*, and *yz* planes through the isocenter) are shown. Red and blue dots indicate locations of the added impulses and the isocenter, respectively. Red lines indicate our axial ROI, which is from 5th to 60th slices (out of 64). Blue line displays the location of the center slice. Finally, green lines show the detector coverage.

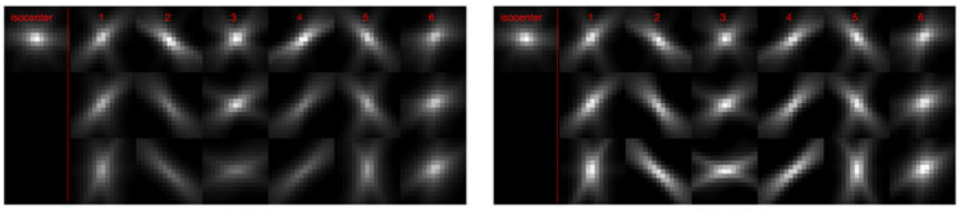


(a) A-REG (b) R-REG

**Fig. 2.**

Comparison of xy plane through the center of each local impulse response at selected location (see Fig. 1 for the index of locations). Quadratic potential function was used. Top row is from a center slice (blue line in Fig. 1), middle row is from 1st slice of ROI (red line in Fig. 1), and bottom row is from outside ROI (green line in Fig. 1). (a) Regularization with original aggregated certainty (6) (A-REG) (b) Regularization with proposed pre-tuned spatial strength (38) (R-REG).

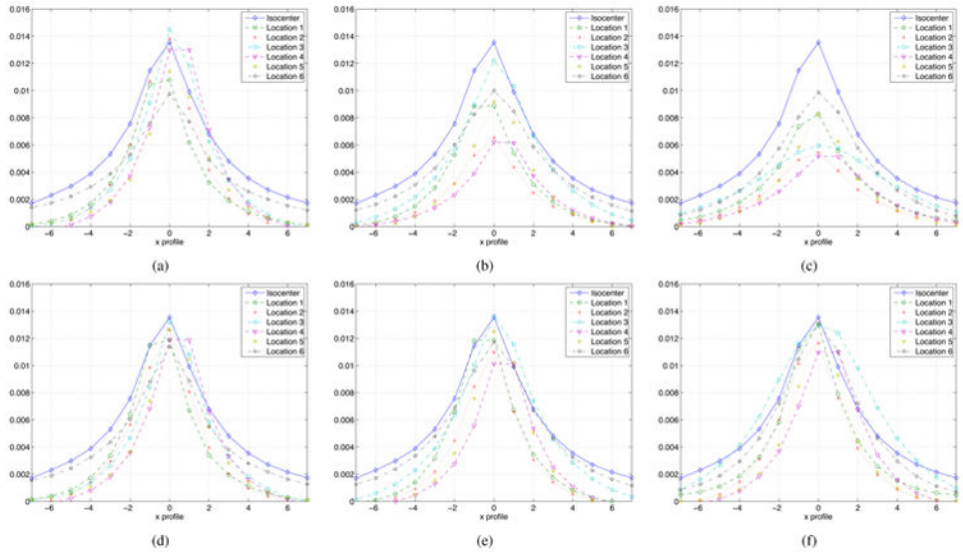


**Fig. 3.**

Comparison of x profiles through the center of each impulse response in Fig. 2. Left column is from a center slice, middle column is from 1st slice of ROI, and right column is from outside of ROI. Top and bottom rows represent the regularizers A-REG (6) and the proposed R-REG (38), respectively. (a) A-REG, center slice (b) A-REG, 1st slice of ROI (c) A-REG, outside ROI (d) R-REG, center slice (e) R-REG, 1st slice of ROI (f) R-REG, outside ROI.

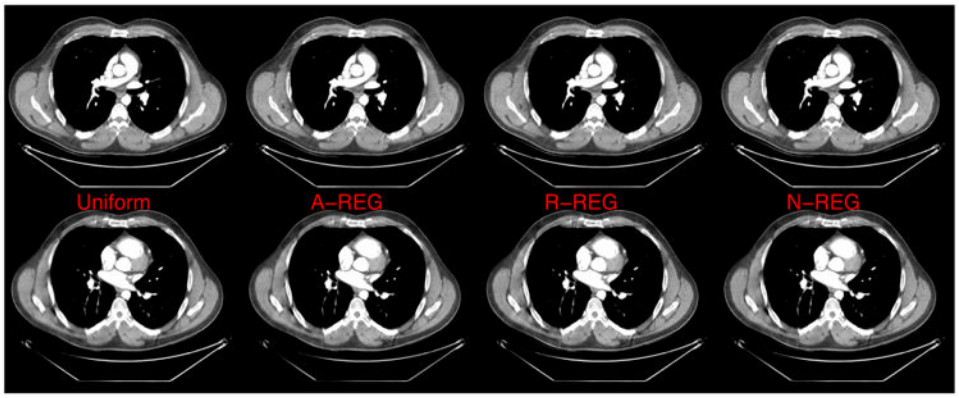


**Fig. 4.**

Reconstructed images using uniform regularizer (1st column), A-REG (2nd column), R-REG (3rd column), and N-REG (last column). Quadratic potential function was used. Top row: center slice; bottom row: the last slice of ROI. Display range is [800 1200] (HU).

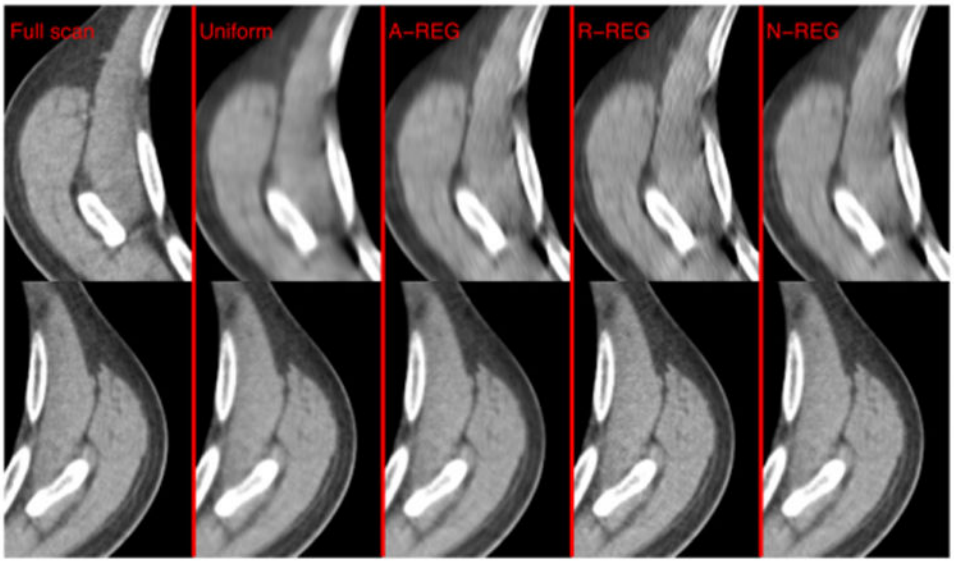


**Fig. 5.**

Comparison of reconstructed images in Fig. 4 at the last slice of ROI. From left to right, the images are from full scan measurements with A-REG, uniform regularizer, A-REG, R-REG, and N-REG, respectively. Top row is from a region on the left side where sampling is lower than a region on the right side (bottom row). Display range is [800 1200] (HU).

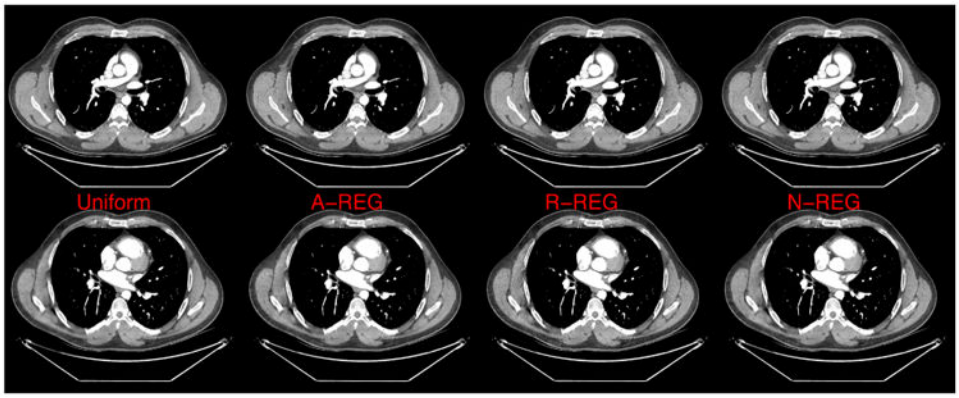


**Fig. 6.**

Reconstructed images using uniform regularizer (1st column), A-REG (2nd column), R-REG (3rd column), and N-REG (last column). Edge-preserving potential function (54) was used. Top row: center slice; bottom row: the last slice of ROI. Display range is [800 1200] (HU).

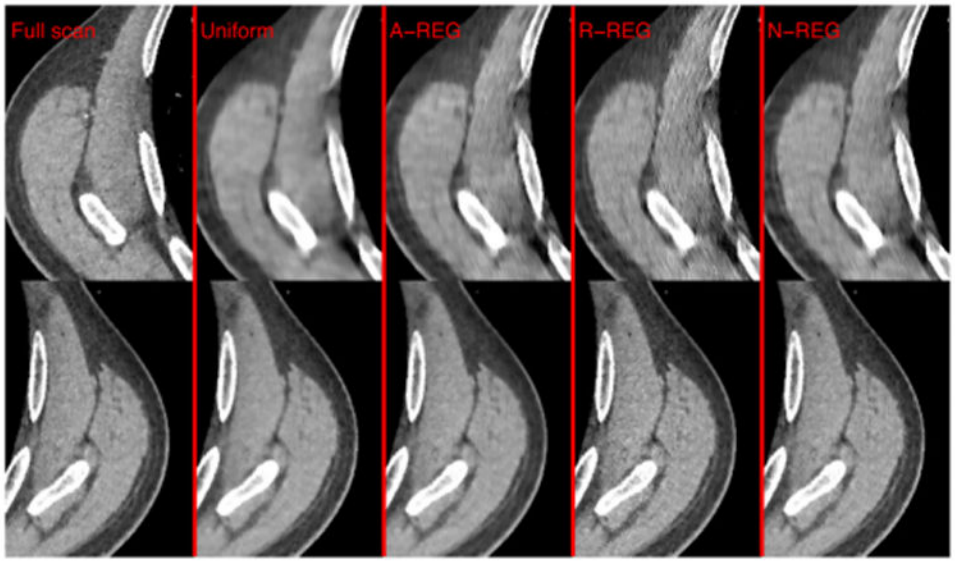


**Fig. 7.**

Comparison of reconstructed images in Fig. 6 at the last slice of ROI. From left to right, the images are from full scan measurements with A-REG, uniform regularizer, A-REG, R-REG, and N-REG, respectively. Top row is from a region on the left side where sampling is lower than a region on the right side (bottom row). Display range is [800 1200] (HU).

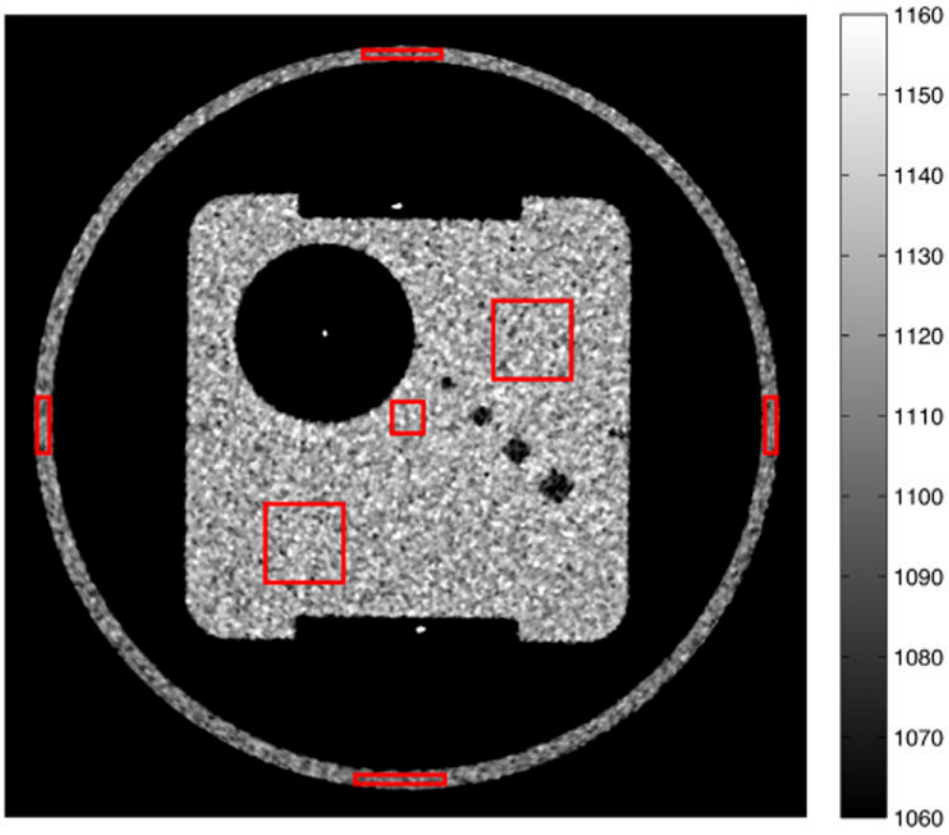


**Fig. 8.**

The GEPP used for quantitative comparison of regularizations. Red boxes indicate the regions selected for noise variance comparison.

**Table I**

**Acronyms for regularizers**

| Acronym | Description |
|---|---|
| A-REG | aggregated certainty (AC) regularizer (6) |
| R-REG | regularizer for spatial resolution uniformity (38) |
| N-REG | regularizer for noise uniformity (51) |

**Table II**

Average CRC mismatch (52) for selected 6 locations across slices and within each slice, respectively (Units: %). See Fig.1 for the index of impulse locations.

| | Locations | | | | | | Averages | | | |
|---|---|---|---|---|---|---|---|---|---|---|
| | **1** | **2** | **3** | **4** | **5** | **6** | **Overall** | **Center Slice** | **1st slice of ROI** | **Outside ROI** |
| A-REG (Fig. 3) | 32.6 | 45.3 | 24.8 | 47.2 | 31.9 | 25.0 | 34.5 | (a) 12.3 | (b) 33.7 | (c) 46.8 |
| R-REG (Fig. 3) | 7.5 | 14.9 | 3.9 | 20.0 | 5.9 | 7.2 | 9.9 | (d) 8.7 | (e) 11.6 | (f) 7.4 |

**Table III**

Comparison of the noise standard deviation for different regularizers method. All values are in Hounsfield units (HU).

| | Uniform | A-REG | R-REG (38) | N-REG (51) |
|---|---|---|---|---|
| Plexiglas™ Insert (center) | 14.0 | 13.7 | 13.7 | 13.6 |
| Plexiglas™ Insert (right) | 18.8 | 16.0 | 16.2 | 16.4 |
| Plexiglas™ Insert (left) | 15.1 | 14.4 | 14.5 | 14.9 |
| Phantom Wall (left) | 15.4 | 9.3 | 9.5 | 11.8 |
| Phantom Wall (right) | 16.9 | 8.8 | 6.8 | 10.1 |
| Phantom Wall (top) | 17.4 | 8.7 | 8.8 | 10.7 |
| Phantom Wall (bottom) | 16.1 | 7.7 | 8.8 | 10.9 |
| Average | 16.2±1.6 | 11.2±3.4 | 11.2 ±3.6 | 12.6 ±2.4 |